Chinese Chemical Letters 32 (2021) 1121–1126

Contents lists available at ScienceDirect

Chinese Chemical Letters

journal homepage: www.elsevier.com/locate/cclet

Communication

# Stable confinement of Fe/$Fe_3C$ in Fe, N-codoped carbon nanotube towards robust zinc-air batteries

Lingbo Zong[a], Xin Chen[a], Shuming Dou[b], Kaicai Fan[c,*], Zumin Wang[d], Wenjun Zhang[a], Yunmei Du[a], Jie Xu[b], Xiaofei Jia[a], Qi Zhang[a], Xia Li[a], Yida Deng[b], Yanan Chen[b,*], Lei Wang[a]

[a] *Taishan Scholar Advantage and Characteristic Discipline Team of Eco Chemical Process and Technology, Key Laboratory of Optic-electric Sensing and Analytical Chemistry for Life Science, MOE, State Key Laboratory of Eco-chemical Engineering, College of Chemistry and Molecular Engineering, Qingdao University of Science and Technology, Qingdao 266042, China*

[b] *School of Materials Science and Engineering, Key Laboratory of Advanced Ceramics and Machining Technology of Ministry of Education, Tianjin Key Laboratory of Composite and Functional Materials, Tianjin University, Tianjin 300072, China*

[c] *Centre for Clean Environment and Energy, School of Environment and Science, Griffith University, Queensland 4222, Australia*

[d] *Institute of Process Engineering, Chinese Academy of Sciences, Beijing 100190, China*

ARTICLE INFO

*Article history:*
Received 14 July 2020
Received in revised form 9 August 2020
Accepted 13 August 2020
Available online 19 August 2020

*Keywords:*
Patial confinement
Nonprecious metal
Bifunctional
Oxygen electrocatalyst
Synergistic effect Zn-air batterie

ABSTRACT

Catalytic oxygen reduction reaction (ORR) and oxygen evolution reaction (OER) have garnered great attention as the key character in metal-air batteries. Herein, we developed a superior nonprecious bifunctional oxygen electrocatalyst, fabricated through spatial confinement of Fe/$Fe_3C$ nanocrystals in pyridinic N and Fe-$N_x$ rich carbon nanotubes (Fe/$Fe_3C$-N-CNTs). During ORR, the resultant electrocatalyst exhibits positive onset potential of 1.0 V (*vs.* RHE), large half-wave potentials of 0.88 V (*vs.* RHE), which is more positive than Pt/C (0.98 V and 0.83 V, respectively). Remarkably, Fe/$Fe_3C$-N-CNTs exhibits outstanding durability and great methanol tolerance, exceeding Pt/C and most reported nonprecious metal-based oxygen reduction electrocatalysts. Moreover, Fe/$Fe_3C$-N-CNTs show a markedly low potential at $j$ =10 mA/cm$^2$, small Tafel slopes and extremely high stability for OER. Impressively, the Fe/$Fe_3C$-N-CNTs-based Zn-air batteries demonstrate high power density of 183 mW/cm$^2$ and robust charge/discharge stability. It is revealed that the spatial confinement effect can impede the aggregation and corrosion of Fe/$Fe_3C$ nanocrystals. Meanwhile, Fe/$Fe_3C$ and Fe-$N_x$ play synergistic effect on boosting the ORR/OER activity, which provides an important guideline for construction of inexpensive nonprecious metal-carbon hybrid nanomaterials.

Electrochemical oxygen reduction reaction (ORR) and oxygen evolution reaction (OER) have attracted great interests as a vital process of metal-air batteries and fuel cells [1,2]. The commercialization of these energy conversion and storage devices prominently relies on the manufacture of low cost, highly active and stable ORR/OER electrocatalysts [3]. At present, the most widely employed ORR/OER electrocatalysts are noble metal-based materials. Unfortunately, relative scarcity, high cost, poor durability and susceptibility to poisoning have impeded practical applications of noble metal-based materials [4]. Thus, great efforts are needed to develop cost effective and earth abundant electrocatalysts with comparable or even better electrocatalytic activity for ORR/OER than that of precious metal-based materials.

To date, numerous nonprecious metal bifunctional oxygen electrocatalysts have been developed, including heteroatoms-doped carbon nanomaterials [5,6], metal oxides [7–9], metal oxides supported on carbon materials and transition metal-nitrogen-carbon materials (TM-N-Cs, TM = Fe, Co) [10–12], *etc.* Especially, TM-N-Cs show exceptional catalytic activities towards ORR, which are better or comparable to benchmark precious metals [13]. However, most of them presents far from satisfactory catalytic activity and stability towards OER, owing to the serious deterioration of principal features of active sites, including electrochemical oxidation or defunctionalization of carbon atoms located at edges/defects sites or reversible adsorption of oxygen groups on carbon atoms adjacent to TM-$N_x$ sites in the potential range for OER [14–16]. Recently, tremendous efforts have been

---

[*] Corresponding authors.
*E-mail addresses:* kaicai.fan@griffithuni.edu.au (K. Fan), yananchen@tju.edu.cn (Y. Chen).

https://doi.org/10.1016/j.cclet.2020.08.029
1001-8417/

devoted to alleviate the degradation of active sites, such as introducing proper foreign atom into carbon or integrating metal-based nanoparticles with well-defined graphitized carbon [17–19]. Amongst, transition metal particles encapsulated in nitrogen doped carbon (M@NC) have been highlighted as fabulous bifunctional oxygen electrocatalyst, which is likely to be used in zinc-air battery [18,19].

Recently, carbon nanotubes (CNTs) accompanied with intrinsically remarkable electrical conductivity, high chemical stability and unique structural features become attractive when used as matrix for nonprecious metal and noble metal electrocatalysts for ORR/OER [20,21]. CNTs-based hybrids are beneficial to increase the number of active centers, promote the mass transportation and improve electrochemical corrosion resistance [22–24]. By taking advantage of the high surface area and porous nanostructures, CNTs as well as the rich active sites exhibit excellent electrocatalytic performance [25]. Apart from the above aspect, TM-$N_x$ active sites bonded or linked on CNTs can boost the electrocatalytic activity by the rapidly electron transfer from current collector to catalytically active sites [26]. Notably, CNTs shells encapsulated transition metal nanocrystals provide remarkable ORR activity because of the electron transfer from metal nanoparticles to carbon shells, leading to the decreased work function on carbon shell surface [27]. Moreover, recent investigations elucidate that nitrogen doping is an effective strategy to hinder the corrosion and enhance the stability of carbon-based materials through modifying the charge distribution in the carbon rings. Increasing the doping level of nitrogen cannot only augment the exposure of catalytic active sites but also stabilize the carbon-based support, thus boosting the performance of the electrocatalysts [28]. However, very few progress have been made in employing CNTs as carbon matrix for Fe-N-C electrocatalysts because of the tedious processes of surface treatment [29]. In these regards, controllable fabrication of Fe and N doped CNTs with stable spatial confined Fe/$Fe_3C$ as bifunctional electrocatalyst for ORR/OER is desirable. Therefore, it is still fascinating and challenging to explore facile and cost-effective strategy to prepare non-noble metal-based oxygen electrocatalysts with decent activity, proper architecture and excellent interaction between carbon and Fe/$Fe_3C$ nanocrystals.

In this study, we present a scalable and straightforward approach to produce highly active ORR/OER electrocatalyst: Fe, N-doped nanotubes with spatial confined Fe/$Fe_3C$ nanocrystals. Through pyrolysis, the *in situ* generated Fe/$Fe_3C$ nanocrystals are well spatial confined by Fe, N-doped CNTs. In this spatial confinement effect, steric effect can impede the corrosion and aggregation of Fe/$Fe_3C$ nanocrystals in harsh medium during electrocatalysis. The in-depth investigation indicates that Fe/$Fe_3C$ nanocrystals can dramatically boost the electrocatalytic activity of active sites. The synergetic effect between Fe-$N_x$ active sites, Fe/$Fe_3C$ nanocrystals and Fe, N-doped CNTs architecture elevates electrocatalytic activity of Fe/$Fe_3C$-N-CNTs bifunctional oxygen electrocatalyst. Notably, the fabricated rechargeable Zn-air batteries possess large powder density of 183 mW/$cm^2$, excellent durability of 195 h and small charge-discharge voltage gap of 0.81 V.

Materials: Melamine (Sigma Aldrich), Nafion solution (Sigma Aldrich), $NaNO_3$, $FeCl_3 \cdot 6H_2O$, KOH and HCl (Sinopharm Chemical Reagent Co., Ltd.), 20 wt% commercial Pt/C and 99.95% $RuO_2$ (Alfa Aesar). All chemicals were used without further purification.

Efficient Fe/$Fe_3C$-N-CNTs bifunctional oxygen electrocatalyst was synthesized using straightforward sol-gel approach. Firstly, 1.2 g glucose and 1.6 g $NaNO_3$ were firstly dissolved in 30 mL DI water to form a homogeneous solution. Melamine (1.2 g) was dump in and stirred for 10 min. Secondly, 6 mL HCl (0.5 mol/L) and 10 mL $FeCl_3$ (0.5 mol/L) solution were added into the solution to form homogeneous supramolecular hydrogel, and the formed hydrogel state was stabilized through holding for 12 h. The resulted products were washed with Milli-Q water and freeze dried. And then they were heated in $N_2$ atmosphere 800 °C for 1 h (gas flow rate: 50 sccm, 5 °C/min). The obtained products were then washed thoroughly by Milli-Q water to wipe off the remained NaCl impurity and subsequently freeze dried. The final oxygen electrocatalyst denoted as Fe/$Fe_3C$-N-CNTs was collected for further characterization and test.

The N-doped carbon materials (N-C) electrocatalyst was fabricated according to the strategy for preparing Fe/$Fe_3C$-N-CNTs without introduction of $FeCl_3 \cdot 6H_2O$.

The obtained electrocatalysts were characterized using Scanning electron microscope (SEM, FE-SEM, S4800, Hitachi), transmission electron microscope (TEM, JEM-2100 F), high angle annular dark field scanning transmission electron microscope (HAADF-STEM) and powder X-ray diffraction (XRD Rigaku-Dmax 2500 diffractometer with Cu-K$\alpha$ radiation, $\lambda$ = 0.15405 nm). The chemical compositions and chemical valence state were inspected by X-ray photoelectron spectroscopy (XPS, Kratos Axis ULTRA). The specific surface area of the result electrocatalysts were characterized using nitrogen adsorption/desorption at 77 K (Micromeritics ASAP 2020 physisorption analyzer). Raman spectroscopy was obtained on the confocal Raman microscope with the laser wavelength of 532 nm (LabRAM HR800).

The electrochemical performance was conducted on electrochemical workstation (Gamry, USA), which equipped with the Pine' RDE (rotational disk electrode, D = 5 mm) and RRDE (ring-disk electrode, D = 5.61 mm). The rotating glassy carbon electrode was polished by $Al_2O_3$. The catalyst ink was prepared by mixing 5.0 mg of electrocatalysts in the mixed solution (730.0 $\mu$L of water, 240.0 $\mu$L of isopropanol and 30.0 $\mu$L of Nafion). The electrocatalyst loading was 0.510 mg/$cm^2$.

Glassy carbon electrode with electrocatalysts, Ag/AgCl (saturated KCl) and graphite rod were applied as working electrode, reference electrodes and counter electrodes, respectively. 0.1 mol/L KOH or 0.5 mol/L $H_2SO_4$ solution was used as electrolyte solution. For comparison, the commercial Pt/C electrocatalyst ink was also prepared. The ORR performance was evaluated by bubbling the alkaline electrolyte with high purity $O_2$. The working electrode was cycled 50 circles at a scan rate of 50 mV/s before the measurement. The LSV polarization curves were performed from 1.2 V to 0.2 V (*vs.* RHE) with different electrode rotating rates (scan rate of 5 mV/s). All the obtained LSV polarization curves were corrected with iR-correction.

For the calculation of $H_2O_2$% and electron transfer number (n), RRDE measurement was conducted in $O_2$ saturated 0.1 mol/L KOH and the Pt ring electrode potential was constant at 1.2 V (*vs.* RHE). The $H_2O_2$% and *n* were calculated by the following equations:

$$n = \frac{4I_{\text{disk}}}{I_{\text{ring}}/N + I_{\text{disk}}} \tag{1}$$

$$H_2O_2\% = \frac{200I_{\text{ring}}/N}{I_{\text{ring}}/N + I_{\text{disk}}} \tag{2}$$

Here, $I_{\text{disk}}$ and $I_{\text{ring}}$ were the disk current and ring current, and $N$ = 0.37 was the current collection efficiency of Pt ring.

The glassy carbon electrode (D =5 mm, 0.196 $cm^2$) loaded with resulted electrocatalysts was used as the working electrode, Hg/HgO electrode and graphite rod as reference and counter electrode, respectively. The catalyst loading of $RuO_2$ (or the obtained electrocatalysts) was 0.510 mg/$cm^2$. The LSV were obtained at a scan rate of 5 mV/s and 1600 rpm to alleviate the $O_2$ bubbles on working electrode surface. The recorded potential was converted to the reversible hydrogen electrode (RHE), following the equation of $E_{RHE} = E_{Hg/HgO} + 0.926\,V - 95\%\ iR$ in 1.0 mol/L KOH solution.

The electrocatalyst slurry was prepared by mixing electrocatalysts (5 mg) in isopropanol (950 μL)/Nafion (50 μL) mixed solution, followed by ultrasonication. 6 mol/L KOH solution was used as an electrolyte. Air cathode was fabricated by uniformly coating electrocatalyst slurry onto the carbon paper followed by drying at room temperature. The loading capacity for the obtained electrocatalysts is 1 mg/cm$^2$. Zn plate was used as the anode of the constructed rechargeable Zn-air battery with 6 mol/L KOH solution as electrolyte. The rechargeable Zn-air battery was conducted on home-built cells.

The growth of Fe/Fe$_3$C-N-CNTs is schematically demonstrated in Fig. 1a. Typically, the hydrogel is firstly prepared through forming metal-melamine coordination with the assistance of sodium nitrate. Then, the hydrogel mixture composed of glucose, melamine and FeCl$_3$ is carbonized under the N$_2$ atmosphere for the efficient development of Fe/Fe$_3$C-N-CNTs. During the pyrolysis process, Fe$^{3+}$ is reduced to Fe by the carbothermal reduction reactions and then Fe reacted with the carbon, leading to the hybrid of Fe and Fe$_3$C [30]. X-ray diffraction (XRD) pattern is employed to distinguish the composition of the obtained electrocatalyst. As elucidated in Fig. 1b, Fe/Fe$_3$C-N-CNTs display obvious sharp peaks at 26.0°, 43.7°, 44.7° and 65.0°, which can be assigned undisputedly to (002) plane of graphitic carbon, (102) plane of Fe$_3$C and (110) and (200) planes of Fe, respectively. The XRD results signify that graphitic carbon, Fe and Fe$_3$C consist in Fe/Fe$_3$C-N-CNTs. In this reaction system, glucose provides carbon source for the controlled growth of Fe/Fe$_3$C-N-CNTs catalyzed by iron species [31]. It is revealed that Fe and Fe$_3$C can promote the graphitization of the surrounding carbon, and thus Fe/Fe$_3$C nanocrystals are encompassed by the graphitic carbon.

The morphology of hydrogel precursor is firstly investigated by scanning electron microscopy image (SEM). As shown in Fig. S1 (Supporting information), the aerogel is constructed by smooth and ultralong nanofiber with a diameter of 240 nm. The representational transmission electron microscopy image (TEM) in Fig. 1c further confirms the growth of CNTs, which should be originated from the transportation and realignment of carbon atoms catalyzed by the added iron in the pyrolysis process. The bright-field high-resolution TEM image (HRTEM, Fig. 1d) discloses that iron-containing nanoparticles confined by CNTs are well crystallized with the lattice distance of 0.201 nm (corresponding to the (110) crystallographic plane of cubic metallic Fe (PDF No. 06-696) or (220) plane of Fe$_3$C (PDF No. 35–772). Energy dispersive X-ray mapping (EDX) is also employed to illustrate the different elements distributions. Remarkably, the corresponding High-angle annular dark-field STEM image (HAADF-STEM) of Fig. 1e and element mappings (Figs. 1f–h) reveal highly dispersed Fe, Fe$_3$C nanocrystals and uniform distributions of C, N, Fe elements. The detected Fe signal illustrates the successful dispersion of Fe in N-doped CNTs.

In addition, N$_2$ adsorption/desorption isotherm (Fig. 2a) demonstrates large Brunauer-Emmett-Teller (BET) surface area of Fe/Fe$_3$C-N-CNTs (245.46 m$^2$/g) with meso/macroporous characteristic, favoring the mass transport and exposure of more active sites. Raman spectroscopy is conducted to describe the carbon structure of Fe/Fe$_3$C-N-CNTs, and the corresponding Raman spectra (Fig. 2b) clearly display characteristic D peak (defect band) and G peak (graphite band). As characterized by the intensity ratio of $I_D/I_G$, it suggests that Fe/Fe$_3$C-N-CNTs show lower $I_D/I_G$

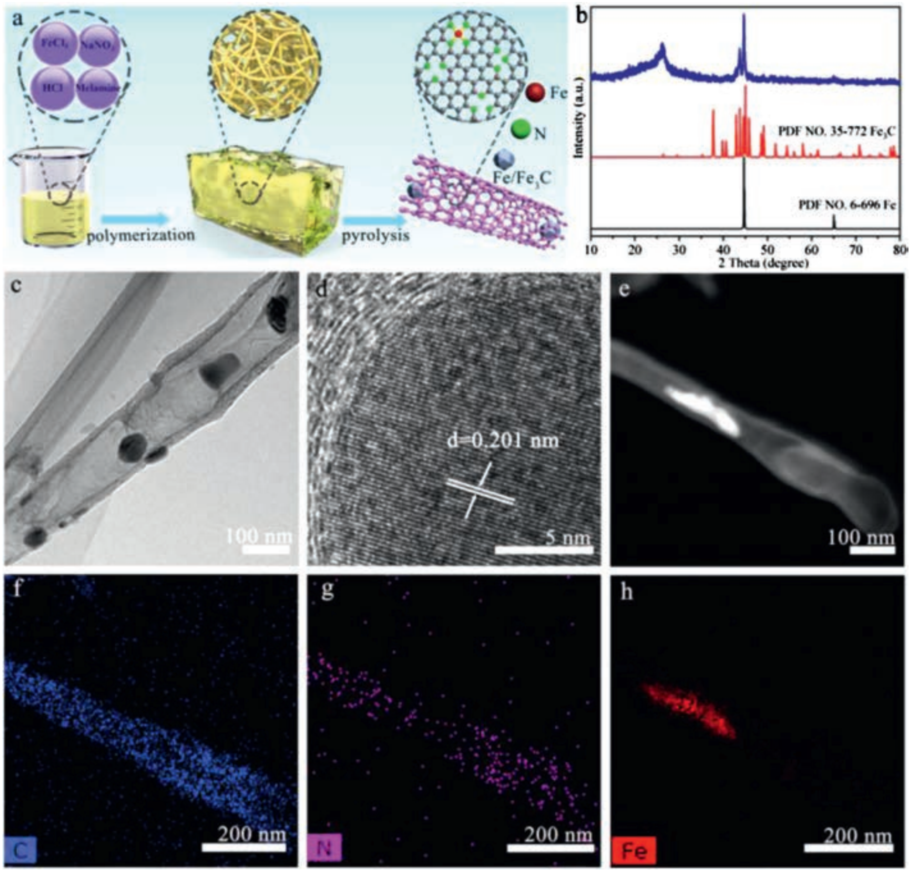

**Fig. 1.** (a) Schematic illustration for the preparation process of Fe/Fe$_3$C-N-CNTs. (b) XRD of Fe/Fe$_3$C-N-CNTs. (c) TEM image. (d) High-magnification TEM image. (e) HAADF-STEM image of Fe/Fe$_3$C-N-CNTs. Corresponding elemental mapping of (f) C, (g) N and (h) Fe.

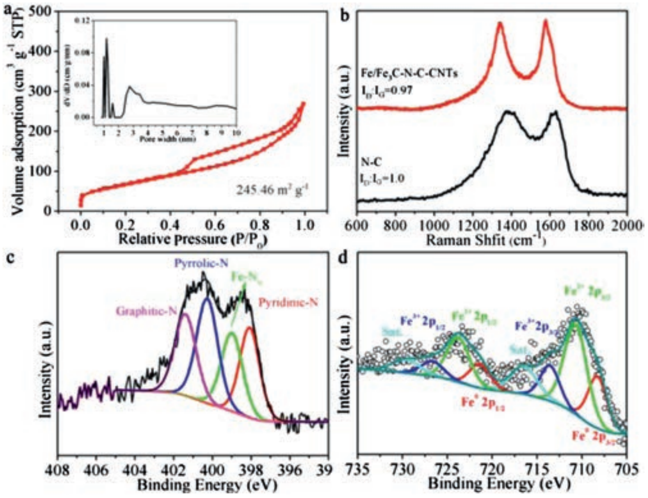

**Fig. 2.** (a) $N_2$ adsorption-desorption isotherms, the pore size distribution curve (inset) of Fe/$Fe_3$C-N-CNTs. (b) Raman spectra of the Fe/$Fe_3$C-N-CNTs and N-C. (c) High-resolution N 1s spectrum of Fe/$Fe_3$C-N-CNTs. (d) The Fe 2p XPS spectrum of Fe/$Fe_3$C-N-CNTs.

(0.97) than N—C (1.0), signifying higher degree of graphitization and excellent electrical conductivity. The improved graphitization degree is attributed to the Fe catalyzed graphitization mechanism in the high temperature pyrolysis process [32]. To further investigate the composition and chemical states of Fe/$Fe_3$C-N-CNTs, X-ray photon spectroscopy (XPS, Fig. 2c) characterization is adopted. The N 1s spectrum indicates the coexistence of graphitic N (401.2 eV), pyrrolic N (399.6 eV), Fe-$N_x$ (399.0 eV) and pyridinic-N (398.1 eV) [33,34]. As shown in Fig. 2d, the high-resolution Fe 2p spectrum indicates that these peaks are identified as $Fe^0$ (708.1 eV), $Fe^{2+}$ (710.7 eV, 723.9 eV), $Fe^{3+}$ (713.6 eV, 726.7 eV) and satellite peak (716.5 eV, 729.6 eV) [35]. It should be noted that the graphitization of carbon is another key factor that influences the stability of the electrocatalyst. Though the Fe-$N_x$ single atom structure is formed at relative low pyrolysis temperature, *e.g.*, 700 °C, the catalytic activity and stability are inferior than the one prepared at higher temperature. The amorphous or low graphitized carbon, which experiences obviously structure decomposition at high oxidizing potentials should be avoided in the prepared electrocatalysts [36,37].

To explore the effect of pyrolysis temperature on ORR activities, the electrocatalytic performance of Fe/$Fe_3$C-N-CNTs pyrolyzed at different temperatures of 700 °C, 800 °C and 900 °C are demonstrated in Fig. S2 (Supporting information). In addition, the $N_2$ adsorption/desorption isotherm curves (Fig. S3 in Supporting information) show similar high specific surface area of 226.3 $m^2$/g for Fe/$Fe_3$C-N-CNTs-700, 245.5 $m^2$/g for Fe/$Fe_3$C-N-CNTs-800, 275.3 $m^2$/g for Fe/$Fe_3$C-N-CNTs-900), thus eliminating the effect of specific surface area on ORR activity. As displayed in Fig. S2, Fe/$Fe_3$C-N-CNTs-800 show the highest $E_{\text{onset}}$ (onset potential), most positive $E_{1/2}$ (half-wave potential), and largest $j$ (limiting current density). The results testify that the pyrolysis temperature at 800 °C seemed to be the optimal temperature in the synthesis of Fe/$Fe_3$C-N-CNTs electrocatalyst. The weak electrocatalytic performance of Fe/$Fe_3$C-N-CNTs-700 may due to the lower graphitization, which is demonstrated by Raman spectra (Fig. S4 in Supporting information). For the Fe/$Fe_3$C-N-CNTs-900, despite the outstanding graphitic degree, they own low N content and poor active N species (pyridinic-N), as illustrated by XPS analysis (Fig. S5, Tables S1 and S2 in Supporting information). Thus, the influence of pyrolysis on electrocatalytic activity may be attributed to the synergistic effect of active N doping and graphitic degree of the electrocatalysts obtained at different pyrolysis temperatures.

Fig. 3a reveals the linear sweep voltammetry (LSV) results of Fe/$Fe_3$C-N-CNTs, N-C and benchmark Pt/C. The LSV curves show that the control electrocatalyst (N-C) displays the worst ORR performance in terms of the onset potential $E_{\text{onset}}$, half-wave potential $E_{1/2}$ and limited current density $j$. Significantly, when Fe/$Fe_3$C nanocrystals are introduced into the carbon matrix, the ORR activity of Fe/$Fe_3$C-N-CNTs dramatically leaped forward according to the largest $E_{\text{onset}}$ (1.0 V) and most positive $E_{1/2}$ (0.88 V), which is 110 mV and 50 mV more positive than that of N-C ($E_{1/2}$ = 0.77 V), benchmark Pt/C ($E_{1/2}$ = 0.83 V), respectively. The superior ORR activity of Fe/$Fe_3$C-N-CNTs is more excellent than that of most nonprecious metal electrocatalysts [38,39] and CNT-based carbon electrocatalysts (Table S3 in Supporting information). The largest $j$ indicates that the conductivity of Fe/$Fe_3$C-N-CNTs is boosted, which may be due to the improvement of graphitization degree in the presence of Fe/$Fe_3$C nanocrystals and N doping during pyrolysis process [40]. The electron transfer number ($n$) for ORR is acquired from LSV curves under different rotation speeds (Fig. 3b) according to the Koutechy-Levich (K–L) plots. The K–L plots (Fig. 3b inset) show good linear relationships, with similar slope of 3.93, confirming a four-electron pathway for ORR process. It is well known that a smaller Tafel slope signifies the faster kinetic process for ORR [41]. Fig. 3c shows the smallest Tafel plots of ~ 84 mV/dec than that of Pt/C (92 mV/dec) and N-C (163 mV/dec) suggesting outstanding ORR kinetics.

To further evaluate the ORR process of Fe/$Fe_3$C-N-CNTs, RRDE measurements is employed. As shown in Fig. 3d, Fe/$Fe_3$C-N-CNTs indicate high disk current density for ORR and much lower ring current density for $H_2O_2$ oxidation. Fig. S6 (Supporting information) reveals the electron transfer numbers ($n$) and $H_2O_2$% calculated from the RRDE curves. As shown in Fig. S6, the $H_2O_2$% is strikingly suppressed by Fe/$Fe_3$C-N-CNTs, and the $H_2O_2$% is lower than 10%. The large electron transfer number ($n$) for Fe/$Fe_3$C-N-CNTs indicates that Fe/$Fe_3$C-N-CNTs possess highly efficient four-electron transfer process and superior electrocatalytic efficiency. Thus, the analysis results illustrate that it is all-important to introduce Fe/$Fe_3$C nanocrystals into the material for attaining exceptionally high performance, which can facilitate the formation of Fe-$N_x$ active species. In addition, the stability and methanol tolerance are also explored. Notably, Fe/$Fe_3$C-N-CNTs show strong long-term durability than Pt/C, as attested by the slower decay rate of the chronoamperometry measurement (Fig. 3e). After 20,000 s stability test, the TEM image of Fe/$Fe_3$C-N-CNTs displays exceptional morphological stability (Fig. S7 in Supporting information), elucidating the encouraging stability of the as-synthesis electrocatalyst. After the injection of methanol into the electrolyte solution, the current density of benchmark Pt/C decrease rapidly, whereas no significant change of Fe/$Fe_3$C-N-CNTs (Fig. 3f). These experimental results unambiguously testify that Fe/$Fe_3$C-N-CNTs own excellent methanol tolerance much better than and superior stability stronger than benchmark Pt/C. The superior ORR activity of Fe/$Fe_3$C-N-CNTs under alkaline electrolyte stimulates us to study the ORR performance in 0.5 mol/L $H_2SO_4$ acidic media. As shown in Fig. S8a (Supporting information), it is demonstrated that the $E_{\text{oneset}}$ (0.84 V) of Fe/$Fe_3$C-N-CNTs is only 60 mV lower than the benchmark Pt/C (0.90 V). Remarkably, Fe/$Fe_3$C-N-CNTs exhibit strong robustness in acidic media, as disclosed by the very weak decay (5%, 1600 rpm) after 20,000 s continuous cycles (Fig. S8b in Supporting information).

To demonstrate the difunctional performance, we further evaluate the OER activity of the Fe/$Fe_3$C-N-CNTs in 1.0 mol/L KOH solution. LSV curves of the samples are recorded at 5 mV/s, 1600 rpm. As displayed in Fig. 4a, the LSV of N—C presents the largest onset potential (1.68 V) of OER at $j$ =10 mA/$cm^2$, indicating

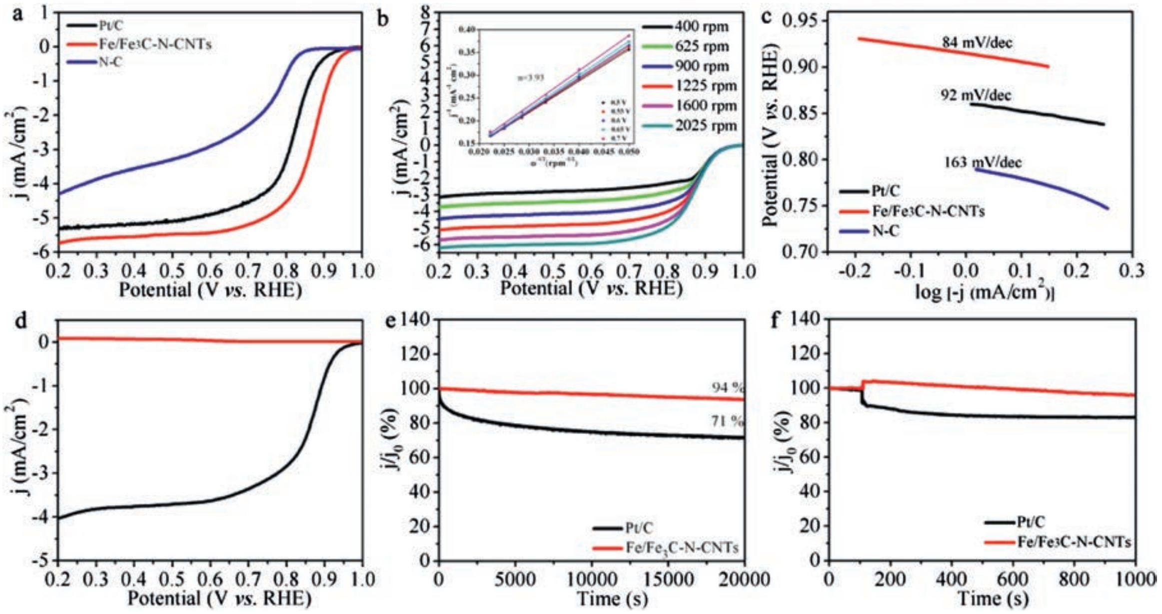

**Fig. 3.** (a) LSV curves of Pt/C, Fe/$Fe_3C$-N-CNTs and N-C. (b) LSV curves under different rotation speeds (600-2025 rpms) for Fe/$Fe_3C$-N-CNTs with 5 mV/s. inset: K-L plots at different potentials. (c) Tafel plots of ORR for Pt/C, Fe/$Fe_3C$-N-CNTs and N-C. (d) ORR polarization curves measured by using RRDE technique at 1600 rpm, 5 mV/s. (e) Chronoamperometric curves of Pt/C, Fe/$Fe_3C$-N-CNTs at 0.6 V (*vs.* RHE), 1600 rpm. (f) Chronoamperometric response of Pt/C, Fe/$Fe_3C$-N-CNTs upon addition of 2.0 mol/L methanol at 0.6 V *vs.* RHE.

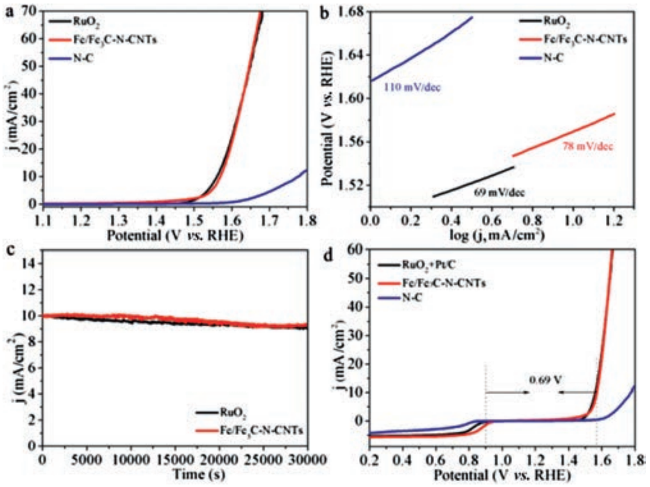

**Fig. 4.** (a) Polarization curves of Fe/$Fe_3C$-N-CNTs, N-C and $RuO_2$ for OER. (b) Tafel plots from the LSV curves. (c) Chronoamperometric curves of Fe/$Fe_3C$-N-CNTs, N-C and Pt/C with 10 mA/cm$^2$ in 1.0 mol/L KOH, 1600 rpm. (d) The potential gap of Fe/$Fe_3C$-N-CNTs.

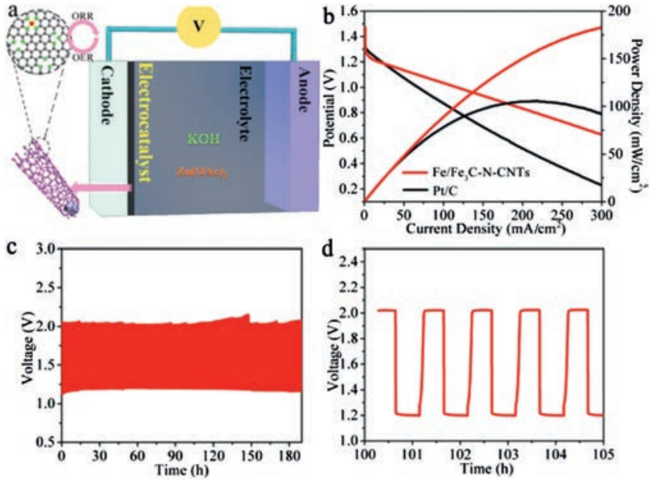

**Fig. 5.** (a) Schematic illustration of the Zn-air batteries. (b) Polarization curves and power density plots of Zn-air batteries based on Fe/$Fe_3C$-N-CNTs and commercial Pt/C electrodes. (c, d) Galvanostatic charge-discharge cycling curve at the current density of 5 mA/cm$^2$.

the inferior activity. The onset potential decreases rapidly and the anodic current density increases rapidly when Fe/$Fe_3C$ nanocrystals are introduced into the carbon matrix. The superior OER activity of Fe/$Fe_3C$-N-CNTs is reflected by the lower potential of 1.57 V at $j$ =10 mA/cm$^2$ and much higher currents density. It has been demonstrated that pyridinic N electron-withdrawing functional groups can facilitate OER reaction [17]. Thus, Fe/$Fe_3C$-N-CNTs with higher pyridinic N show better OER activity than N—C. The OER kinetics of the electrocatalysts are further analyzed by the Tafel curves as exhibited in Fig. 4b. The Tafel slope of Fe/$Fe_3C$-N-CNTs is 78 mV/dec, which is similar to $RuO_2$ (69 mV/dec), suggesting the extremely exceptional OER kinetics. More noteworthy, Fe/$Fe_3C$-N-CNTs reserve more that 95% of its initial current density (Fig. 4c) even after 30,000 s long-term testing, strongly confirming the excellent robustness of the electrocatalyst. The Fe/$Fe_3C$-N-CNTs after 30,000 s durability test are characterized by TEM (Fig. S9 in Supporting information). The TEM image exhibits no obvious change of morphology, demonstrating excellent stability during the electrochemical testing. The potential gap ($\Delta E$) between the OER potential at $j$ =10 mA/cm$^2$ and $E_{1/2}$ for ORR is adopted to estimate the electrocatalytic performance of bifunctional oxygen electrocatalyst [42]. As reported, a better bifunctional oxygen electrocatalysts tend to have a smaller $\Delta E$. Remarkably, as can be seen in Fig. 4d, Fe/$Fe_3C$-N-CNTs elucidate an exceptionally low $\Delta E$ of 0.69 V, which is much smaller than that $RuO_2$, Pt/C and many reported bifunctional oxygen electrocatalysts [43,44]. Therefore, the newly fabricated Fe/$Fe_3C$-N-CNTs bifunctional oxygen electrocatalyst further elucidate the exceptional activity for both ORR and OER, which confirm the huge potential as outstanding air cathode electrocatalyst for Zn-air batteries.

To evaluate the potential energy conversion application of Fe/$Fe_3C$-N-CNTs, rechargeable Zn-air batteries are assembled (Fig. 5a) by using Fe/$Fe_3C$-N-CNTs as air cathodes. As shown in Fig. 5b, the assembled Zn-air batteries deliver the polarization and power density curves of Zn-air batteries, and Zn-air batteries with Fe/$Fe_3C$-N-CNTs air cathodes have the larger peak power density of 183 mW/cm$^2$ than that of Pt/C based air cathodes (110 mW/cm$^2$), indicating remarkable performance of the Zn-air batteries. Furthermore, Zn-air batteries assembled with Fe/$Fe_3C$-N-CNTs reveal a much higher discharge current compared to benchmark Pt/C, confirming the outstanding catalytic activity of Fe/$Fe_3C$-N-CNTs [45,46]. The recharge ability and robustness of Zn-air batteries is of great significance for large-scale applications, and the stability is assessed by galvanostatic charge-discharge cycling displayed in Figs. 5c and d. It indicates that the Fe/$Fe_3C$-N-CNTs electrode displays very stable charge and discharge potential even after 195 h (cycle for 195 h: 2.0 V for charging, 1.19 V for discharging), indicating the ultrahigh electrocatalytic stability of Fe/$Fe_3C$-N-CNTs bifunctional oxygen electrocatalyst.

In conclusion, high-performance nonprecious metal Fe/$Fe_3C$-N-CNTs bifunctional oxygen electrocatalyst with high density Fe-$N_x$ sites, active N species and spatial confined Fe/$Fe_3$ nanocrystals for ORR/OER is developed by a simple sol-gel approach and followed pyrolysis tactics. Due to the architectural and componential characteristics, the obtained Fe/$Fe_3C$-N-CNTs exhibit remarkable electrocatalytic performance in both alkaline and acidic electrolyte, including positive ORR $E_{\text{onset}}$, large ORR $E_{1/2}$ and the lower potential of OER at $j$ =10 mA/cm$^2$. Experimental results reveal that the remarkable catalytic activities attribute to the synergistic effect of confined Fe/$Fe_3C$ nanocrystals and intrinsic Fe-$N_x$ active sites as well as the porous network of carbon matrix. Furthermore, Zn-air batteries based on Fe/$Fe_3C$-N-CNTs air electrode exhibit high peak power density of $\sim$ 183 mW/cm$^2$, excellent discharge current and charge-discharge durability ($\sim$ 195 h). Consequently, this finding not only offers feasible approach towards excellent ORR/OER and Zn-air batteries but also presents a reliable technique to prepare new dispersed metal-$N_4$ active sites electrocatalysts for energy conversion.

## Declaration of competing interest

The authors declare that there is no conflict of interest.

## Acknowledgments

This work was supported financially by the National Natural Science Foundation of China (Nos. 51702180, 21703116, 91963113, 51372127), The Scientific and Technical Development Project of Qingdao, China (No. 18-2-2-52-jch), The Taishan Scholar Advantage and Characteristic Discipline Team of Eco Chemical Process and Technology.

## Appendix A. Supplementary data

Supplementary material related to this article can be found, in the online version, at doi:https://doi.org/10.1016/j.cclet.2020.08.029.

## References

[1] J. Zhang, Z. Zhao, Z. Xia, L. Dai, Nat. Nanotechnol. 10 (2015) 444–452.
[2] C. Guan, A. Sumboja, W. Zang, et al., Energy Storage Mater. 16 (2019) 243–250.
[3] H.J. Qiu, P. Du, K. Hu, et al., Adv. Mater. 31 (2019) 1900843.
[4] J. Wu, H. Zhou, Q. Li, et al., Adv. Energy Mater. 9 (2019) 1900149.
[5] H. Jiang, J. Gu, X. Zheng, et al., Energy Environ. Sci. 12 (2019) 322–333.
[6] L. Chen, X. Xu, W. Yang, J. Jia, Chin. Chem. Lett. 31 (2020) 626–634.
[7] W. Wang, L. Kuai, W. Cao, et al., Angew. Chem. Int. Ed. 56 (2017) 14977–14981.
[8] Y. Jiang, K. Dong, Y. Lu, et al., Sci. China Mater. 63 (2020) 1247–1256.
[9] X. Zhao, J. Meng, Z. Yan, F. Cheng, J. Chen, Chin. Chem. Lett. 30 (2019) 319–323.
[10] Z.S. Wu, S. Yang, Y. Sun, et al., J. Am. Chem. Soc. 134 (2012) 9082–9085.
[11] Z. Jiang, W. Sun, H. Shang, et al., Energy Environ. Sci. 12 (2019) 3508–3514.
[12] X. Chen, X. Zhen, H. Gong, et al., Chin. Chem. Lett. 30 (2019) 681–685.
[13] B.Q. Li, C.X. Zhao, S. Chen, et al., Adv. Mater. 31 (2019) 1900592.
[14] J. Li, M. Chen, D.A. Cullen, et al., Nat. Catal. 1 (2018) 935–945.
[15] Z. Liu, Z. Zhao, Y. Wang, et al., Adv. Mater. 29 (2017) 1606207.
[16] L. Bai, C.S. Hsu, D.T.L. Alexander, H.M. Chen, X. Hu, J. Am. Chem. Soc. 141 (2019) 14190–14199.
[17] H.B. Yang, J. Miao, S.F. Hung, et al., Sci. Adv. 2 (2016) 1501122.
[18] T. Tang, W.J. Jiang, X.Z. Liu, et al., J. Am. Chem. Soc. 142 (2020) 7116–7127.
[19] G. Wu, K.L. More, C.M. Johnston, P. Zelenay, Science 332 (2011) 443–447.
[20] K. Gong, F. Du, Z. Xia, M. Durstock, L. Dai, Science 323 (2009) 760–764.
[21] B. Chen, G. Sun, J. Wang, et al., Chem. Commun. 56 (2020) 5131–5134.
[22] P.J. Wei, G.Q. Yu, Y. Naruta, J.G. Liu, Angew. Chem. Int. Ed. 53 (2014) 6659–6663.
[23] J.C. Li, P.X. Hou, C. Shi, et al., Carbon 109 (2016) 632–639.
[24] S. Yasuda, A. Furuya, Y. Uchibori, J. Kim, K. Murakoshi, Adv. Funct. Mater. 26 (2016) 738–744.
[25] C. Zhu, S. Fu, J. Song, et al., Small 13 (2017) 1603407.
[26] R. Cao, R. Thapa, H. Kim, et al., Nat. Commun. 4 (2013) 2076–2082.
[27] D. Deng, L. Yu, X. Chen, et al., Angew. Chem. Int. Ed. 52 (2013) 371–375.
[28] Y. Li, W. Zhou, H. Wang, et al., Nat. Nanotechnol. 7 (2012) 394–400.
[29] Y.J. Sa, D.J. Seo, J. Woo, et al., J. Am. Chem. Soc. 138 (2016) 15046–15056.
[30] Z. Wen, S. Ci, F. Zhang, et al., Adv. Mater. 24 (2012) 1399–1404.
[31] D. Xia, X. Yang, L. Xie, et al., Adv. Funct. Mater. 29 (2019) 1906174.
[32] Z. Zhang, J. Sun, F. Wang, L. Dai, Angew. Chem. Int. Ed. 57 (2018) 9038–9043.
[33] W. Zang, A. Sumboja, Y. Ma, et al., ACS Catal. 8 (2018) 8961–8969.
[34] H.W. Liang, W. Wei, Z.S. Wu, X. Feng, K. Mullen, J. Am. Chem. Soc. 135 (2013) 16002–16005.
[35] L. Lin, Q. Zhu, A.W. Xu, J. Am. Chem. Soc. 136 (2014) 11027–11033.
[36] B.Y. Xia, Y. Yan, N. Li, et al., Nat. Energy 1 (2016) 15006–15013.
[37] Y. Zhang, J. Zai, K. He, et al., Chem. Commun. 54 (2018) 3158–3161.
[38] P. Yin, T. Yao, Y. Wu, et al., Angew. Chem. Int. Ed. 55 (2016) 10800–10805.
[39] B.Y. Guan, L. Yu, X.W. Lou, Energy Environ. Sci. 9 (2016) 3092–3096.
[40] W.J. Jiang, L. Gu, L. Li, et al., J. Am. Chem. Soc. 138 (2016) 3570–3578.
[41] M. Xiao, H. Zhang, Y. Chen, et al., Nano Energy 46 (2018) 396–403.
[42] S. Chen, J. Duan, Y. Zheng, et al., Energy Storage Mater. 1 (2015) 17–24.
[43] Q. Liu, Y. Wang, L. Dai, J. Yao, Adv. Mater. 28 (2016) 3000–3006.
[44] T.Y. Ma, J. Ran, S. Dai, M. Jaroniec, S.Z. Qiao, Angew. Chem. Int. Ed. 54 (2015) 4646–4650.
[45] C. Wang, N.H. Xie, Y. Zhang, et al., Chem. Mater. 31 (2019) 1023–1029.
[46] W. Liu, J. Zhang, Z. Bai, et al., Adv. Funct. Mater. 28 (2018) 1706675.